A Mesoscale Modeling Study of the Atmospheric Circulation of High Southern Latitudes*

KEITH M. HINES

Polar Meteorology Group, Byrd Polar Research Center, The Ohio State University, Columbus, Ohio

DAVID H. BROMWICH

Polar Meteorology Group, Byrd Polar Research Center, and Atmospheric Sciences Program, The Ohio State University, Columbus, Ohio

THOMAS R. PARISH

Department of Atmospheric Science, University of Wyoming, Laramie, Wyoming

(Manuscript received 7 March 1994, in final form 4 August 1994)

ABSTRACT

The meteorology of high southern latitudes during winter is simulated using a cloud-free version of The Pennsylvania State University–National Center for Atmospheric Research Mesoscale Model version 4 (MM4) with a 100-km horizontal resolution. Comparisons between idealized simulations of Antarctica with MM4 and with the mesoscale model of Parish and Waight reveal that both models produce similarly realistic velocity fields in the boundary layer. The latter model tends to produce slightly faster drainage winds over East Antarctica. The intensity of the katabatic winds produced by MM4 is sensitive to parameterizations of boundary layer fluxes. Two simulations are performed with MM4 using analyses from the European Centre for Medium-Range Weather Forecasts for June 1988 as initial and boundary conditions. A simulation of the period from 0000 UTC 2 June to 0000 UTC 8 June produces realistic synoptic phenomena including ridge development over East Antarctica, frontogenesis over the Amundsen Sea, and a katabatic surge over the Ross Ice Shelf. The simulated time-averaged fields for June 1988, particularly that of a 500-hPa height, are in good agreement with time-averaged fields analyzed by the European Centre for Medium-Range Weather Forecasts. The results of the simulations provide detailed features of the Antarctic winter boundary layer along the steeply sloping terrain. Highest boundary layer wind speeds averaged over the month-long simulation are approximately 20 m s^{-1}. The lack of latent heating in the simulations apparently results in some bias in the results. In particular, the cloud-free version of MM4 underpredicts the intensity of lows in the sea level pressure field.

1. Introduction

In this paper, we examine the success of a version of The Pennsylvania State University–National Center for Atmospheric Research (Penn State–NCAR) Mesoscale Model version 4 (MM4) in simulating features of the meteorology of high southern latitudes. The climate of high southern latitudes is largely controlled by the unique characteristics of the Antarctic continent. Antarctica is a massive dome of ice, with approximately 70% of its surface being above 2000 m in elevation. Perhaps the most remarkable features of the regional climate are the extremely low temperatures over the East Antarctic plateau and the persistent katabatic winds over much of the continent. Katabatic winds are noted for their high directional constancy, which exceeds 0.9 in many locations. Intense longwave radiative cooling over the sloping ice terrain drives the regional circulation. Furthermore, links have been suggested between Antarctica's katabatic winds and offshore mesoscale cyclogenesis (e.g., Bromwich 1991), as well as with the tropospheric circulation over the continent (James 1988) and the Southern Ocean (Yasunari and Kodama 1993).

Fastest katabatic speeds are located along the steep coastal escarpment of Antarctica. The relationship between terrain and drainage wind intensity is demonstrated by Ball (1960). He shows that magnitude of the terrain-induced pressure gradient force is directly proportional to both the steepness of the terrain and the inversion strength in the lower troposphere. Coriolis turning of the drainage flow results in a net easterly component of the flow over Antarctica and nearby oceans. The climatological katabatic streamlines of Parish and Bromwich (1987) indicate that broad-scale,

* Contribution 916 of Byrd Polar Research Center.

Corresponding author address: Dr. Keith M. Hines, Byrd Polar Research Center, The Ohio State University, 108 Scott Hall, 1090 Carmack Road, Columbus, OH 43210-1002.

© 1995 American Meteorological Society

topographic features induce extensive confluence in the boundary layer flow. Cape Denison, in a region of confluence along the Adélie Coast, has a yearly averaged wind speed of 19.7 m s^{-1} (Mather and Miller 1967).

It is becoming increasingly clear that mesoscale processes play a critical role in the atmospheric circulation in Antarctic latitudes. This situation is particularly important where stable air is affected by high, steep topography. For example, the ubiquitous barrier winds, with a lateral dimension on the order of 200 km, are a frequent occurrence along the eastern side of the Antarctic Peninsula (Schwerdtfeger 1979). These cold, mountain-parallel winds are part of a circulation responsible for the transport of ice and cold water from the western Weddell Sea into the South Atlantic Ocean. These considerations motivate the study of the circulation near Antarctica with a mesoscale model. The use of MM4 allows for higher resolution of the regional climate-producing features, including topography and sea-ice distribution, than is typically available in studies using only a general circulation model (GCM).

Xu et al. (1990) find that several key features of the climate of high southern latitudes, including the split jet near New Zealand and the intensity of the circumpolar trough, were not adequately simulated by the GCMs analyzed in their study. Tzeng et al. (1993) document the successes and shortcomings of the simulation of Antarctic climate by the NCAR Community Climate Model version 1 (CCM1). The shortcomings include excessive precipitation over the Antarctic continent and winter surface temperatures exceeding observed values by 10–15 K over the interior of the continent. The authors suggest that the misplaced circumpolar trough and the absence of a pronounced split in the Pacific jet stream during winter in CCM1 simulations can be related to the Antarctic katabatic wind circulation.

Observational studies of the Antarctic planetary boundary layer (PBL) indicate features that should be captured in successful modeling studies. These features include the surprisingly large magnitude sensible heat fluxes that frequently occur despite stable stratification within the surface-based inversion. Stearns and Weidner (1993) derived sensible heat fluxes from observations during 1984–90 at a network of automatic weather stations (AWS). Data from two stations routinely yielded downward-directed, monthly averaged heat fluxes in excess of 60 W m^{-2}. Yet, computed vertical diffusivities, hence, the vertical heat flux, are quite small in the upper boundary layer (e.g., Yimin 1992). These considerations suggest that a substantial cooling occurs in the katabatic layer due to divergence of turbulent heat flux as heat lost to the surface is not replenished from above. Parish and Bromwich (1991) noted the large contribution of turbulent flux divergence when they specified combined radiative and turbulent cooling in their modeled one-layer PBL to vary from about 110 W m^{-2} at sea level to about 70 W m^{-2} over the high plateau.

The goal of this study is to develop a mesoscale atmospheric model for Antarctica for climate studies. The mesoscale model should be capable of both being coupled with a GCM for combined regional and global studies or being run independently using analyzed fields for the boundary conditions. The explicit resolution of mesoscale features should improve the simulation of the regional climate. Many studies have demonstrated that coupling a mesoscale model with a GCM can improve simulated precipitation over complex terrain (e.g., Giorgi and Bates 1989; Pitman et al. 1991; Giorgi et al. 1994). The model used in this study has the added capability of analyzing synoptic events during relatively short-term simulations. To the knowledge of the authors, no previously published study has evaluated the meteorology of the entire Antarctic domain with mesoscale simulations using initial conditions and time-varying boundary conditions based upon observations or analyzed fields. It is our intent to show the dominance of dry processes within the dynamics of the Antarctic atmosphere during winter. Consequently, the version of the model used here is completely cloud free.

An advantage of modeling studies is that they can give us realistic patterns of boundary layer quantities in regions of relatively steep topography where surfaces of constant pressure intersect the PBL and the earth's surface. This is particularly important for Antarctica during winter due to the intense surface inversion. A description of the mesoscale model is given in section 2. Comparisons between simulations with MM4 and simulations with the mesoscale model of Parish and Waight (1987) are presented in section 3, along with results of simulations with MM4 for 6 days during and for the month of June 1988. Conclusions based on the simulations and a discussion of future work are presented in section 4.

2. Model description

The mesoscale model, MM4, used in the simulations presented here is a three-dimensional (3D), hydrostatic, primitive equation model. The MM4, described in detail by Anthes et al. (1987), is designed to simulate the atmosphere for a wide variety of realistic initial conditions. Moist atmospheric processes are not considered for the simulations presented in this paper. The prognostic variables surface pressure, temperature, and horizontal velocity are horizontally staggered according to the type-B grid (Arakawa and Lamb 1977). The surface temperature is also predicted based upon the surface energy balance. Key parameterizations for the simulation of katabatic winds include those of the PBL and longwave radiation. Other diabatic or viscous processes included in the simulations presented here are horizontal and vertical diffusion of both heat and momentum and dry convective adjustment. Solar radiation

is included in simulations E1 and E2 described in sections 3b and 3c, respectively.

The PBL representation is based upon the high vertical resolution approach of Zhang and Anthes (1982), which includes four regimes for different ranges of static stability. Surface roughness z_0 is set at 0.01 m over the Antarctic continent and 0.001 m over pack ice and the permanent ice shelves. Surface roughness over the open oceans increases as the boundary layer wind speed increases. Minimum roughness over the oceans is 0.0001 m. The diffusion of temperature is adjusted to conserve the turbulent flux of heat in the vertical. The katabatic wind field is quite sensitive to the vertical profile of the vertical eddy diffusivity K_z. Therefore, the profile equation of Brost and Wyngaard (1978) is used for stable stratification within the lowest 2000 m of the atmosphere,

$$K_Z = \frac{k_0 u_* z[1 - (z/h)]^{1.5}}{1 + 4.7(z/L)}, \quad (1)$$

where z is height above ground level (AGL), k_0 is the von Kármán constant, u_* is the friction velocity, L is the Monin–Obukhov length, and h is the height of the boundary layer,

$$h = d\left(\frac{u_* L}{|f|}\right)^{0.5}, \quad (2)$$

where f is the Coriolis parameter, and d, the value of scaled, surface boundary layer depth, is set equal to 0.4. Furthermore, to reduce the downward flow of heat within the inversion in the lower atmosphere, minimum K_z is reduced from the standard MM4 value of 1.0 to 0.1 $m^2 s^{-1}$ in the lowest 1000 m AGL. Above 1 km, minimum K_z increases linearly with height to 1.0 $m^2 s^{-1}$ at 2 km AGL. For unstable stratification or above 2 km AGL, K_z is obtained following Zhang and Anthes (1982). The surface temperature T_g is obtained from the surface energy balance,

$$\frac{\partial T_g}{\partial t} = \frac{1}{C_g}(R_a - R_g - H_s + S_g) - K_m(T_g - T_m), \quad (3)$$

where R_a and R_g are downward and upward longwave radiative fluxes from the atmosphere and the surface, respectively, H_s is sensible heat flux from the surface to the atmosphere, S_g is absorbed shortwave radiation, T_m is substrate temperature, C_g is thermal capacity per unit area of the surface, and K_m is the heat transfer coefficient of the force restore method. Blackadar (1979) recommends $K_m = 8.58 \times 10^{-5}$ s^{-1} for prediction of the diurnal cycle of soil surface temperature. Due to the lack of a diurnal cycle during the polar night and the relatively high insulation of the Antarctic surface, we set K_m at the reduced value of 1.82×10^{-5} s^{-1} used by Parish and Waight (1987). The thermal capacity C_g is 1.649×10^5 J m^{-2} K^{-1} for the Antarctic ice surface. The sensible H_s is heat flux obtained from the relation,

$$H_s = C_p \rho_a k_0 u_* \frac{\theta_g - \theta_a}{\ln(z_a/z_0) - \psi_h}, \quad (4)$$

where C_p is specific heat at constant pressure, ρ is density, θ is potential temperature, ψ_h is a static stability parameter, and the subscripts a and g here refer to the lowest atmospheric level and surface, respectively. Sea-ice concentration is specified over the oceans. For pack-ice grid points, separate values of T_g, T_m, H_s, R_g, and S_g are retained for the ice and water surface fractions. The temperature of the water surface fraction is 271.4 K, which is taken as the freezing point of seawater. Temperatures T_g and T_m of the ice surface fraction are constrained to be less than or equal to 271.4 K.

For the critical longwave radiative processes, we use the clear sky, graybody scheme of Cerni and Parish (1984), which has been shown to produce realistic katabatic winds in simulations of the flow in the vicinity of West Antarctica (Bromwich et al. 1994). This scheme considers the radiative properties of both carbon dioxide and water vapor. For this scheme, relative humidity is taken to be 30% over most of the vertical depth of the atmosphere, with increased relative humidity for pressures near 1000 hPa.

Domains for the MM4 simulations are based upon polar stereographic projections centered at the South Pole and true at 71°S. Figure 1 shows the two domain sizes employed. The inner square, a 5900 km × 5900 km region, is used to simulate the flow over Antarctica under idealized conditions. The outer square, a 7900 km × 7900 km region, is employed for more realistic simulations, which consider the frequent cyclones over the oceans surrounding Antarctica. Contours represent the climatological sea-ice concentration for June. The larger domain includes the climatological locations of the circumpolar trough and sea ice surrounding Antarctica. Initial and boundary conditions for the simulations with the larger domain are obtained from analyses by the European Centre for Medium-Range Weather Forecasts (ECMWF). We employ a horizontal resolution of 100 km, as Parish and Bromwich (1991) have shown that the katabatic winds can be well simulated by a mesoscale model with this spatial resolution. Time-varying prognostic variables are specified at the horizontal boundaries. In the vertical, the terrain-following σ coordinate is used. The top of the model, an isobaric surface, is taken as a material surface.

Climatological monthly sea-ice and sea surface temperature distributions are obtained from the Geophysical Fluid Dynamics Laboratory (GFDL) Global Oceanographic Dataset Atlas. For nonidealized simulations, substrate temperatures and the initial surface temperatures over the Antarctic ice surface are obtained from the ECMWF TOGA (Tropical Ocean Global Atmosphere) dataset. Surface height data are adapted from Drewry (1983). Figure 2 shows geographic features of interest for Antarctica and gives a 3D repre-

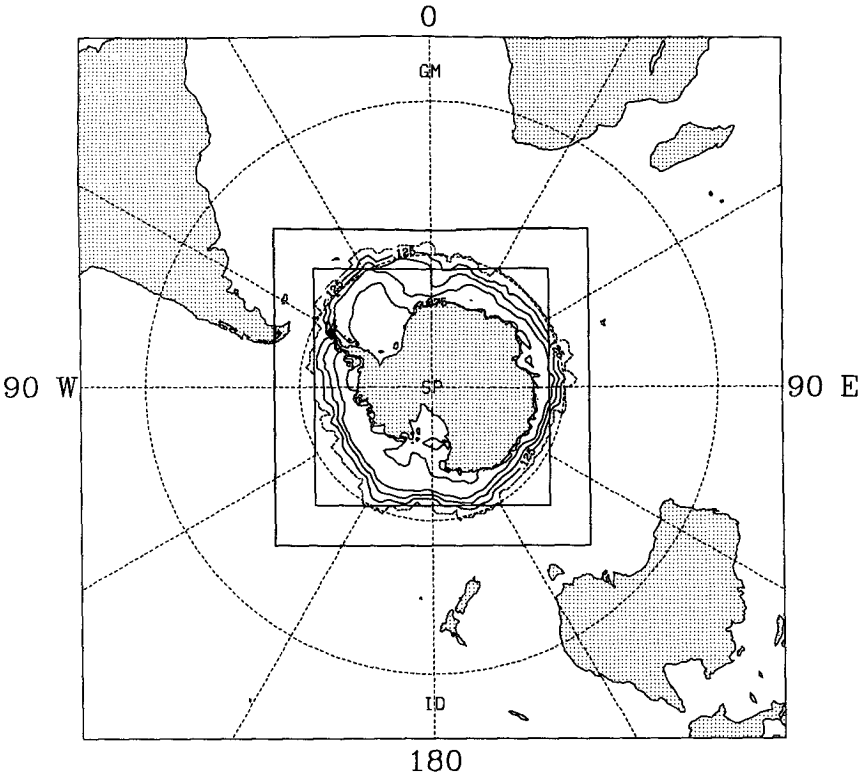

FIG. 1. Horizontal domains for the simulations (squares) and climatological sea-ice concentration for June (contours). The inner square is a 5900 km × 5900 km domain; the outer square is a 7900 km × 7900 km domain. The contour interval for sea-ice concentration is 0.25 starting from 0.125. The dashed line represents the outer edge of the pack ice region.

sentation of the model's topography. The model resolves the flat Ross Ice Shelf and the steep slopes of the Transantarctic Mountains to the southwest. The ridge along the Antarctic Peninsula is present, although considerably smoothed, with this horizontal resolution. Although the representation of the high East Antarctic plateau is quite good, some small-scale features along the coast of East Antarctica are not well represented.

3. Results of the simulations

a. Idealized simulations

We begin by comparing the winds over Antarctica simulated by MM4 against that simulated with a modified version of the mesoscale model described in Parish and Waight (1987). The latter model, hereby referred to as PW, is designed to simulate the flow over Antarctica under idealized conditions, such as starting from a state of rest. Bromwich et al. (1994) demonstrate the success of PW in simulating the katabatic winds in the vicinity of West Antarctica. The PW is identical to MM4 in the staggering of variables in the horizontal and the σ coordinate in the vertical. Furthermore, PW also incorporates the radiation scheme of Cerni and Parish (1984). Unlike MM4, the sensible heat flux H_s is obtained from the similarity method of Businger et al. (1971),

$$H_s = \rho C_p(\overline{\theta'\omega'})_s, \tag{5}$$

where $(\overline{\theta'\omega'})_s$ is obtained from the relation,

$$(\overline{\theta'\omega'})_s^2 - \frac{0.74u_*^3\theta_a}{4.7k_0gz_a}\ln\left(\frac{z_a}{z_0}\right)(\overline{\theta'\omega'})_s - \frac{u_*^4\theta_a}{4.7g}\frac{(\theta_a - \theta_g)}{z_a} = 0, \tag{6}$$

where g is gravity, and z_0 and C_g are set at 0.001 m and 1.649×10^5 J K^{-1} m^{-2}, respectively. Above the surface, turbulent fluxes of heat and momentum in the vertical are from K theory using the diffusivities of Brost and Wyngaard (1978) according to (1).

For this test, the primary emphasis is on the low-level wind field near Antarctica. The horizontal domain, the inner grid shown in Fig. 1, is taken from that of Parish and Bromwich (1991). The polar stereographic domain is discretized into 60 velocity points in the x direction by 60 velocity points in the y direction. In the vertical, there are 10 σ levels concentrated toward the lower atmosphere for both models. Temperature and velocity carried at σ = 0.996, 0.986, 0.97,

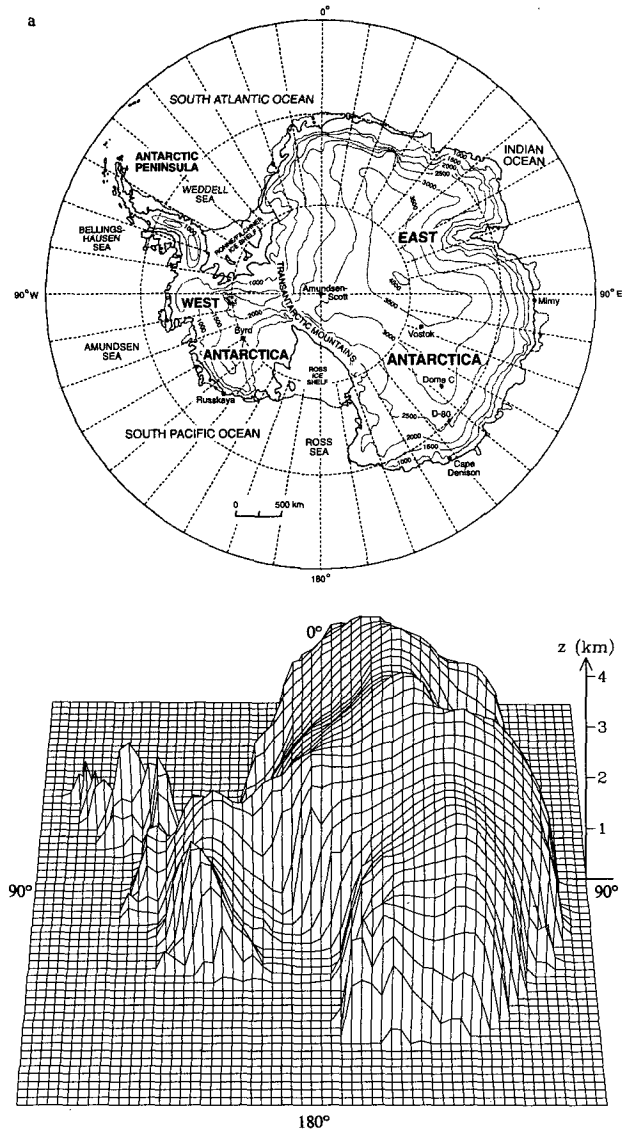

FIG. 2. (a) Location map of Antarctica and surrounding ocean. Thin solid lines are elevation contours at 500-m increments. (b) An isometric view of the Antarctic topography with 100-km resolution as viewed from the 180° meridian.

0.95, 0.925, 0.88, 0.775, 0.5875, 0.35, and 0.1125. Pressure at the model top is 250 hPa. Prognostic variables at the horizontal boundaries are held constant with time in the MM4 simulation, hereby referred to as PB1. To facilitate mixing in the PBL for this simulation only, the bulk Richardson number R_{IB} is reduced by assuming a "synoptic forcing" of a lowest-level wind speed V_L. That is, V_L is given a minimum value of 5 m s^{-1} so that the boundary layer will tend to remain in moderately stable regime 2 as R_{IB}, defined as

$$R_{IB} = \frac{gz_a(\theta_a - \theta_g)}{\theta_a V_L^2}, \qquad (7)$$

will tend to remain below the upper threshold at 0.2. For higher values of R_{IB}, the boundary layer is in the very stable regime 1. In experiments PB2, E1, and E2 discussed later, the minimum value of V_L for (7) is set at 1.0 m s^{-1}. For the simulation, hereby referred to as PW1, corresponding to PB1, but with the model PW, the horizontal velocity is extrapolated linearly to the horizontal boundaries and the boundary temperature is influenced only by radiation and diffusion. In PW1, no assumed forcing was performed in order to produce mixing in the PBL. For both PB1 and PW1, the idealized initial conditions, including the horizontally uniform vertical temperature profile and the zero velocity field, are taken from Parish and Bromwich (1991). For simplicity, ocean surfaces are completely ice covered. The duration of the simulations, 48 h, is long enough to permit the velocity field in the lowest two levels to achieve a quasi-steady state. Table 1 presents a brief summary of the simulations described in this paper.

Figure 3 shows vertical profiles of atmospheric temperature at different stages during the simulation PB1. Profiles are given for the following selected grid points located near the highest point of the East Antarctic plateau (80.59°S, 78.69°E), at the South Pole (90°S), along the coastal escarpment near the Adélie Coast (67.19°S, 143.13°E), and over the ice-covered Pacific Ocean (58.16°S, 135.00°W). The bottom-most temperature shown in the panels of Fig. 3 is the surface temperature. For each site, the warmest profile shown is the initial temperature profile. The initial profile can be taken to represent conditions under which clearing has just occurred after radiation from clouds has disturbed the typical winter inversion profile.

Temperature profiles become progressively cooler as the cloud-free simulation progresses. Early in the simulation, the surface cools rapidly due to outgoing longwave radiation. For all four sites, roughly half the ice surface cooling during the simulation takes place in the first 6 h. Moreover, approximately 90% of the ice surface cooling during the simulation occurs during the first day for the plateau, pole, and ocean sites. As the longwave radiation upwards from the surface decreases, and heat is exchanged by turbulent fluxes between the atmosphere and the cooling surface, the cooling spreads upward within the lower troposphere. Above the third lowest atmospheric level, most of the cooling during PB1 occurs during the second day for the high elevation sites of the East Antarctic plateau and the South Pole. Nevertheless, the cooling is concentrated near the ice surface, rapidly producing strong inversions at all sites displayed in Fig. 3. The smooth, completely frozen surface allows the intensity of the inversion to become unrealistically large over the ocean. Similar to the findings of Parish and Waight (1987), turbulent mixing and horizontal advection noticeably spread the effect of the cooling upward from the surface along the steep coastal escarpment. At hour 48, inversion strength varies from 23 K for the pole to

TABLE 1. Summary of simulations performed.

Simulation	Model	Horizontal domain	Vertical levels	Minimum K_z ($m^2 s^{-1}$)	Initial condition	Period simulated
PW1	PW	$(5900 km)^2$	10	0.1	At rest	2 days
PB1	MM4	$(5900 km)^2$	10	0.1	At rest	2 days
PB2	MM4	$(5900 km)^2$	10	1.0	At rest	2 days
E1	MM4	$(7900 km)^2$	15	0.1	ECMWF	0000 UTC 2 June–0000 UTC 8 June 1988
E2	MM4	$(7900 km)^2$	15	0.1	ECMWF	0000 UTC 1 June–0000 UTC 1 July 1988

12 K for the escarpment. Slightly more than half the inversion strength is concentrated between the surface and the lowest atmospheric level for the plateau, pole, and ocean sites. Interestingly, as the katabatic winds, and consequently increased vertical mixing, develop at the site shown in Fig. 3c, the surface temperature rises almost 5 K from day 1 to day 2 of the simulation.

Concurrent with the cooling of the lower atmosphere is the development of a continent-wide drainage flow. Figure 4 displays the lowest-level horizontal velocity after 48 h of the simulations, PW1 and PB1. The $\sigma = 0.996$ level is roughly 20 m above the surface. Although Fig. 3 demonstrates that the atmosphere continues to cool throughout the simulation, the lowest-level

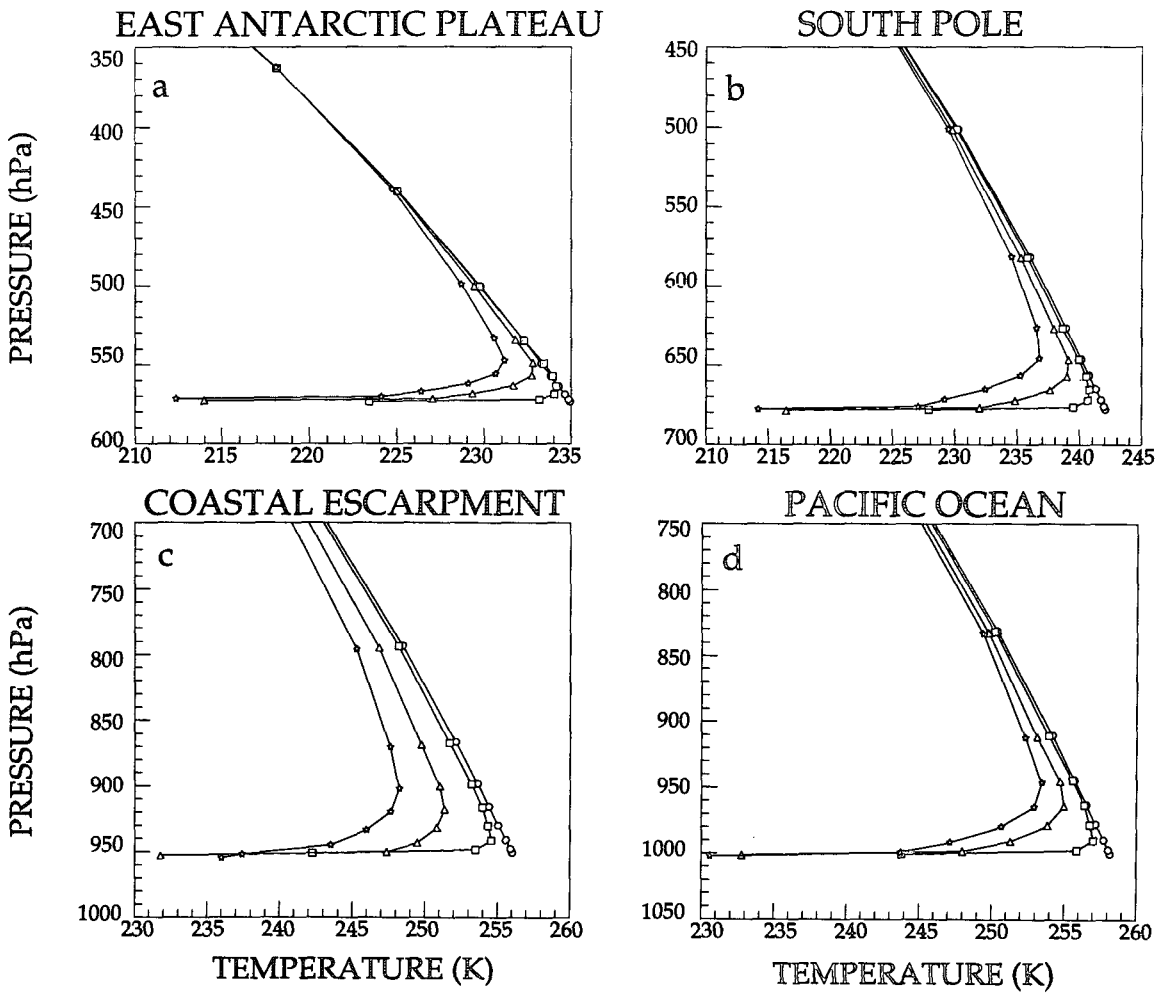

FIG. 3. Vertical profiles of temperature (K, solid lines) for hour 0 (circles), 6 (squares), 24 (triangles), and 48 (stars) of PB1 at four sites: (a) near the top of the East Antarctic plateau (80.59°S, 78.69°E), (b) at the South Pole (90°S), (c) over the coastal escarpment near the Adélie Coast (67.19°S, 143.13°E), and (d) over the ice-covered Pacific Ocean (58.16°S, 135°W).

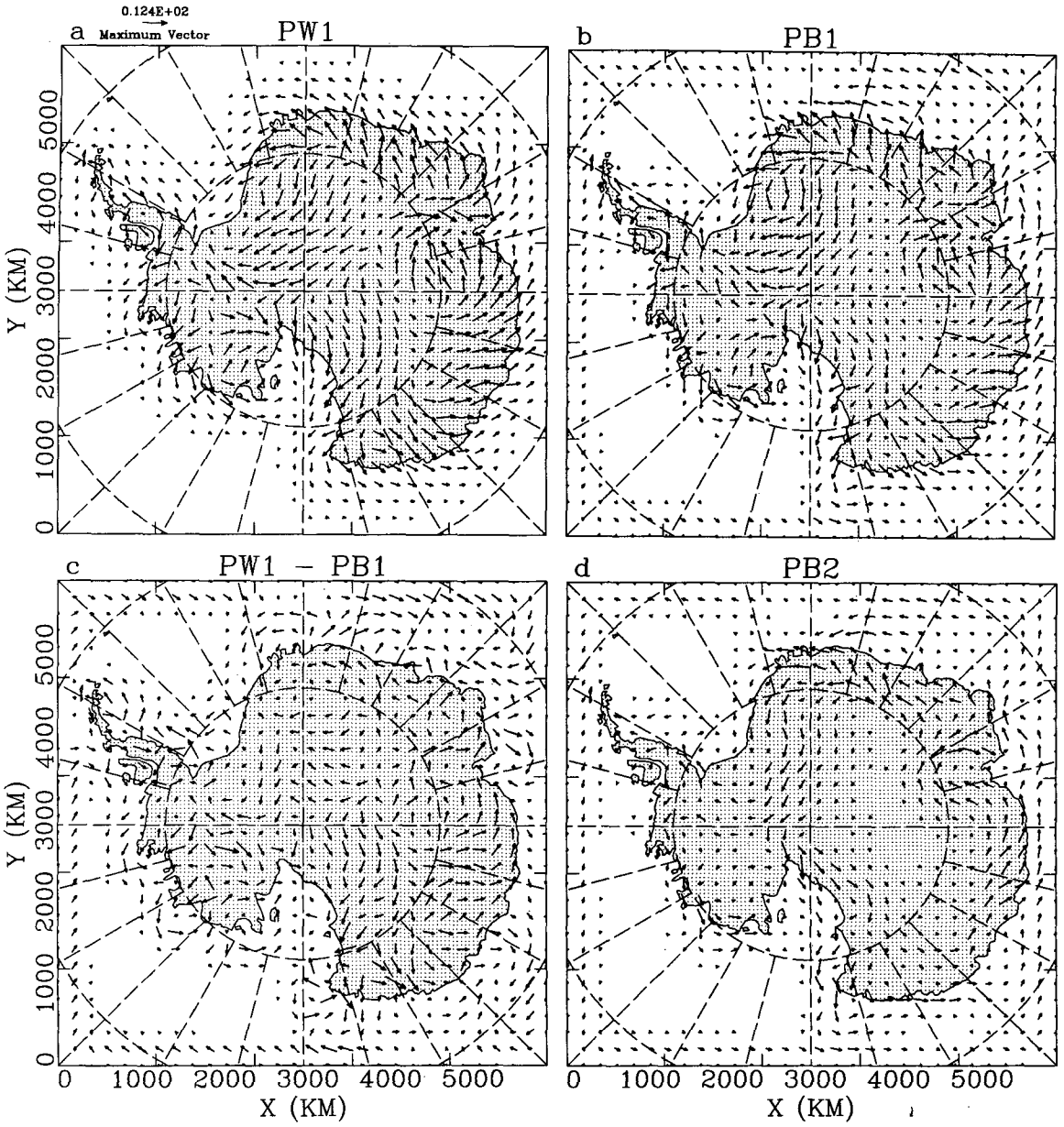

FIG. 4. Horizontal velocity (m s^{-1}, arrows) at the $\sigma = 0.996$ level for hour 48 of (a) PW1, (b) PB1, (c) velocity difference (m s^{-1}, arrows) PW1 − PB1, and (d) PB2.

wind speed becomes quasi-steady after approximately 24 h (not shown). The time development of katabatic winds in idealized simulations is examined by Parish (1992). The wind direction patterns for the velocities shown in Figs. 4a and 4b are quite similar to each other and to that obtained by Parish and Bromwich (1991) in their simulation with a specified constant cooling rate in the PBL. Compare these patterns with the detailed streamline pattern of Parish and Bromwich (1987) displayed in Fig. 5. The latter is obtained from simulations with the diagnostic PBL model of Ball (1960) using a horizontal resolution of 50 km. Both mesoscale simulations PW1 and PB1 clearly produce the continent-scale drainage flow seen in Fig. 5 over East Antarctica as cold low-level air flows from the high plateau to the sea. The flow is deflected to the left by the Coriolis force producing a net easterly component to the flow over Antarctica. In addition, the simulations produce the confluence in West Antarctica upstream of the Ross Ice Shelf and the strong southeasterly flow along the southern edge of the shelf. The mesoscale simulations, however, do not capture many of the fine details of

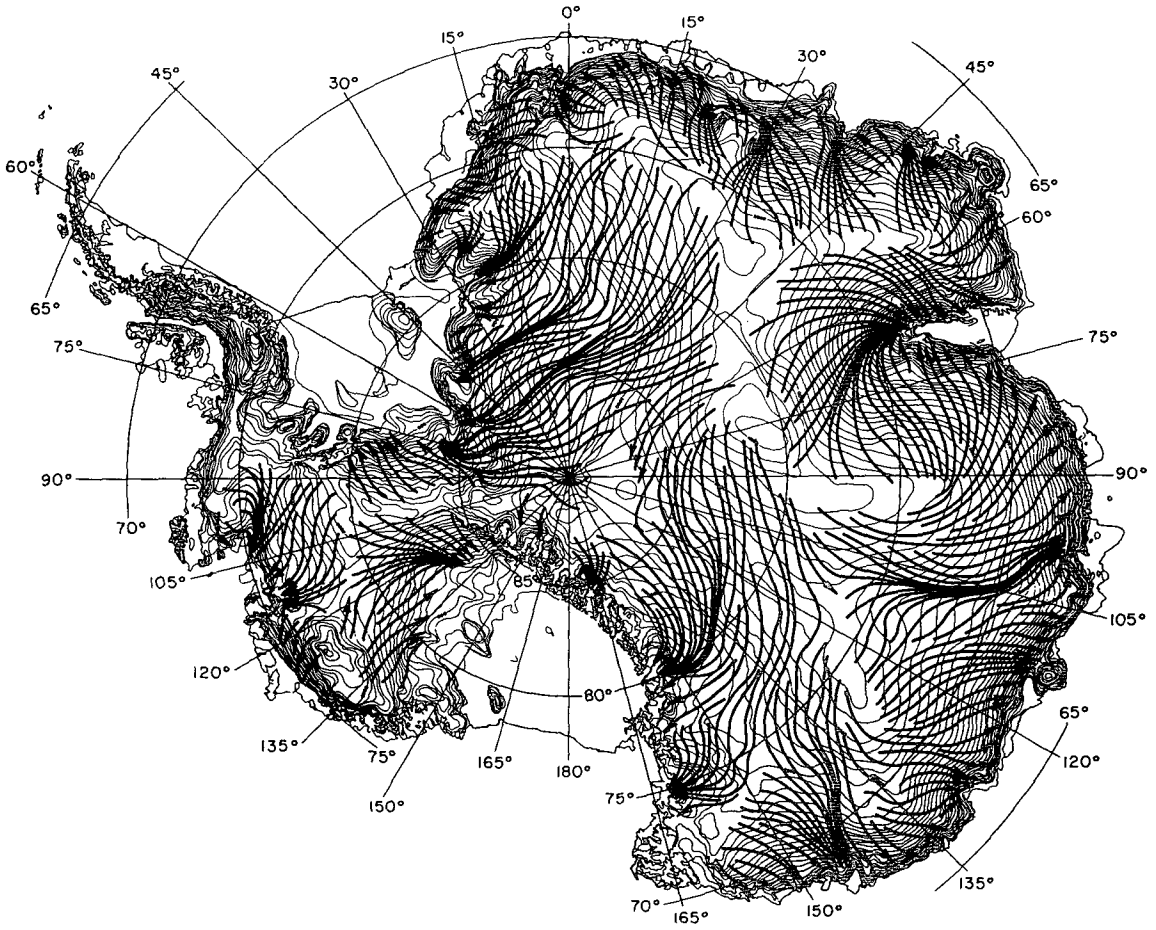

FIG. 5. Simulated streamlines of time-averaged surface winds over Antarctica (heavy lines) from Parish and Bromwich (1987). Thin lines are elevation contours in 100-m increments.

local confluence seen in Fig. 5. They do provide a representation of the flow over a larger area than that shown in Fig. 5. In particular, more details are seen of the flow near the Antarctic Peninsula. Note that the barrier winds along the east side of the peninsula are well captured by PW1 and poorly captured by PB1. Results of additional simulations (not shown) indicate that this difference largely arises from (4) and (5), which determine the sensible heat flux.

Simulated wind speeds are clearly largest over the steep coastal slopes. The PW apparently produces a stronger, more realistic PBL wind field than MM4 in this idealized case, as katabatic speeds tend to be somewhat faster over Antarctica in PW1 than in PB1, although coastal maxima of 13.9 m s^{-1} along the Princess Ragnhild Coast near 30°E and of 11.6 m s^{-1} near the Amery Ice Shelf near 70°E in the latter simulation are larger than the maxima, 11.8 and 10.7 m s^{-1}, respectively, in the former simulation. For grid points with surface elevation between 50 and 3000 m, average lowest-level speeds are 8.0 m s^{-1} for PW1 and 6.9 m s^{-1} for PB1. The difference in speed appears to be especially large for winds over the inland plateau referred to as inversion winds.

The local dependence of MM4 turbulent fluxes on PBL regime type may significantly contribute to the differences between the results of the mesoscale models. Over the inland plateau, where winds are relatively light and R_{IB} is relatively high, the PBL in PB1 tends to stay in the most stable regime 1. Accordingly, the heat flux from the atmosphere to the colder surface is small, almost never exceeding 15 W m^{-2}. Along the steep escarpment, however, wind speeds are larger, consequently, the PBL is typically in regime 2. The sensible heat flux can be quite large in this regime with highest local magnitudes exceeding 80 W m^{-2}. By comparison, highest local magnitudes exceed 100 W m^{-2} in PW1. A large heat flux downward from the atmosphere to the colder surface is critical for the formation and maintenance of strong katabatic winds. Where the low-level wind is relatively fast along the coastal escarpment, the low-level atmospheric cooling due to divergence of the vertical heat flux is often an order of magnitude larger than the cooling due to di-

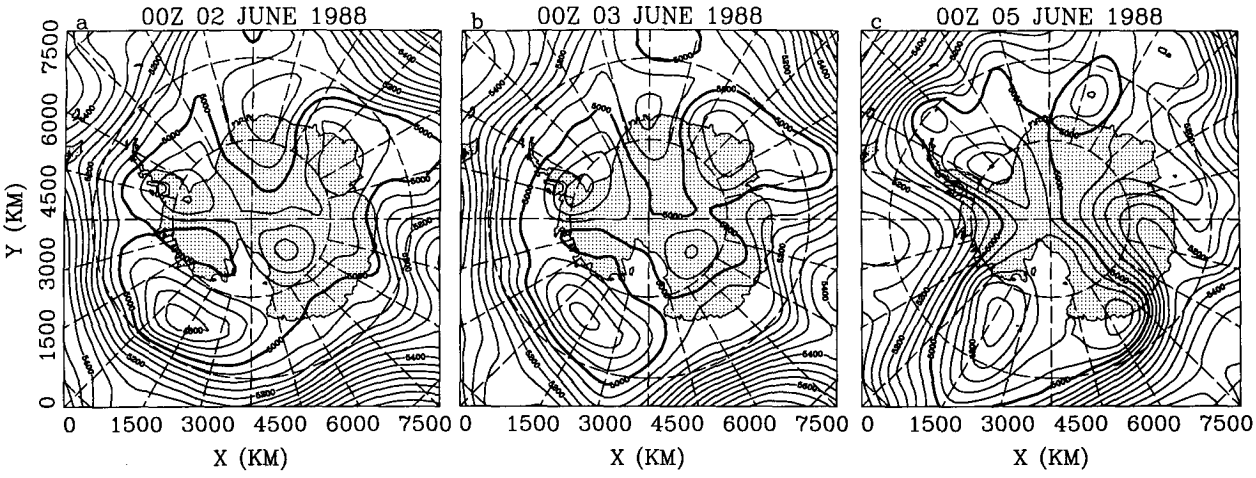

FIG. 6. Maps of the ECMWF analyzed 500-hPa geopotential height (m, solid lines) for (a) 0000 UTC 2 June, (b) 0000 UTC 3 June, and (c) 0000 UTC 5 June 1988. Contour interval is 50 m. Thick contour is 5000 m.

vergence of longwave radiative flux. Thus, by mechanically generating turbulent heat flux, and therefore low-level cooling, the katabatic circulation helps to drive itself.

The importance of both synoptic forcing of boundary layer turbulence and small diffusivities in the vertical in producing simulated katabatic winds is demonstrated with Fig. 4d, which shows the lowest-level velocity for a simulation similar to PB1. In this simulation, referred to as PB2, minimum vertical diffusivity is 1.0 $m^2 s^{-1}$. Furthermore, R_{IB} is not reduced by assuming a synoptic forcing of V_L in this experiment. Consequently, nearly all of the horizontal domain remains in regime 1, and magnitudes of the sensible heat flux are relatively small in PB2. As Fig. 4d shows, the drainage wind speed is considerably weaker in PB2 than that in PW1 and PB1 for the inland plateau and along the Adélie Coast.

In summary, for these idealized conditions, the modified version of MM4 can capture many realistic features of the katabatic flow over Antarctica, although the simulated katabatic speeds appear to be less than observed values. The mesoscale model of Parish and Waight (1987), which is designed specifically for these applications, is slightly more successful.

b. *Synoptic simulation with ECMWF initial and boundary conditions*

The previous simulations have evaluated the success of MM4 in simulating features of the Antarctic climate under idealized conditions. We now simulate the flow for more realistic conditions during the Antarctic winter using ECMWF analyses for both initial and boundary conditions. The intent here is not necessarily to validate the model as a forecast tool, but to show that MM4 simulates realistic behavior in high southern latitudes. Boundary conditions are updated every 12 h from the analyses and interpolated linearly in time between the updates. For the simulation hereby referred to as E1, the horizontal domain is the larger, 7900 km × 7900 km grid displayed in Fig. 1. Thus, cyclones over the pack ice and nearby open ocean are considered in this simulation. The sea-ice concentration for E1 is displayed in Fig. 1. The simulated time period for E1 is from 0000 UTC 2 June to 0000 UTC 8 June 1988. Mesoscale analyses of the meteorological fields are readily available during this time period. A katabatic surge, an increased wind speed event due to synoptically supported katabatic winds from West Antarctica, was observed to develop over the Ross Ice Shelf on 5 June (Carrasco and Bromwich 1993a).

For E1, 15 σ levels are used in the vertical with temperature and velocity carried at σ = 0.996, 0.986, 0.97, 0.95, 0.925, 0.88, 0.815, 0.74, 0.65, 0.55, 0.45, 0.35, 0.25, 0.15, and 0.05. The pressure at the top of model is 100 hPa. Initial temperature is obtained hydrostatically from the ECMWF isobaric height analyses. Initial surface pressure is obtained by an iterative method based on the ECMWF 500-hPa height field and consistent with the model's hydrostatic equation. The initial surface pressure is then adjusted for consistency with the lowest-level wind field. Initial winds are geostrophic.

Figure 6 shows the 500-hPa height field analyzed by ECMWF for 0000 UTC 2 June, 0000 UTC 3 June, and 0000 UTC 5 June. At the time the simulation begins, 0000 UTC 2 June, the 500-hPa height field includes lows to the northeast of the Ross Sea, south of the Antarctic Peninsula, and onshore over East Antarctica. The height gradient over Antarctica tends to be weak compared to the gradient over the Pacific Ocean north of 60°S. Note that a ridge is offshore near 90°E in Fig. 6a. The ridge builds significantly over East Antarctica near 90°E between 3 and 5 June. Figure 7 shows the 500-

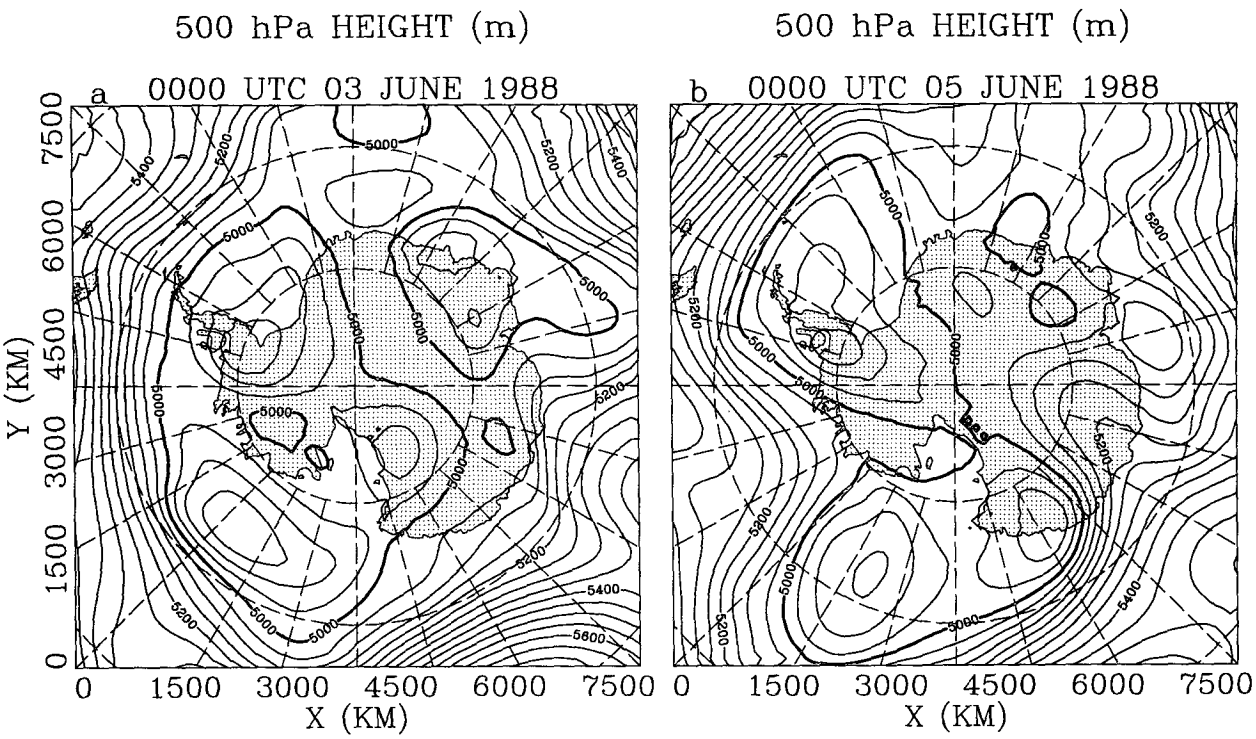

FIG. 7. As in Fig. 6 except for E1 at (a) 0000 UTC 3 June and (b) 0000 UTC 5 June 1988.

hPa height field simulated by MM4 for 0000 UTC 3 June and 0000 UTC 5 June. Clearly, the simulation has captured development of the ridge onto the high terrain of the continent. Other major features of the analyzed 500-hPa height field are also captured in the simulation, although phase error in the simulated location of the troughs and ridges is apparent at 0000 UTC 5 June. Notice that the large ridge over West Antarctica has built too far to the west in E1. Consequently, the simulated low remains near the peninsula, while the corresponding low in the analyses has moved eastward over the Weddell Sea.

Figure 8 shows the sea level pressure field derived from the ECMWF analyses for 0000 UTC 2 June, 0000 UTC 4 June, and 0000 UTC 6 June. From Fig. 8a, it is seen that, at the time of the model's initialization, there

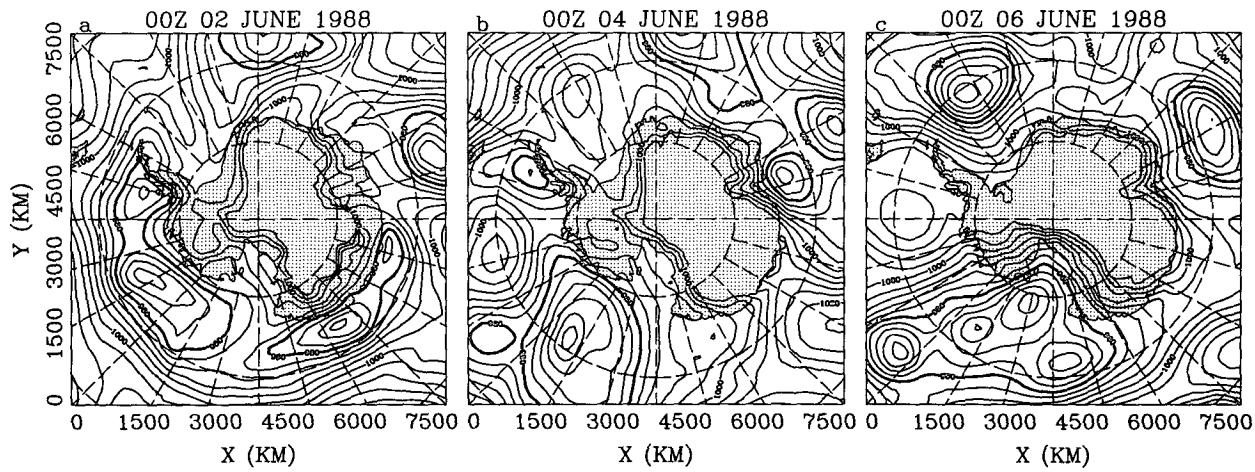

FIG. 8. As in Fig. 6 except for sea level pressure (hPa, solid lines) for (a) 0000 UTC 2 June, (b) 0000 UTC 4 June, and (c) 0000 UTC 6 June 1988. Contour interval is 4 hPa. Thick contour is 980 hPa. Contours are suppressed over high terrain.

is a deep low with a central pressure of 967 hPa near 120°W, which extends west toward the Ross Sea. Another low with a central pressure of 971 hPa is slightly west of the Antarctic Peninsula. The pressure gradient over the Ross Ice Shelf is consistent with modest amplitude geostrophic winds from the southeast. The low near the Antarctic Peninsula propagates to the east during the next 4 days, while the low over the Ross Sea approaches the Ross Ice Shelf from the northeast during 4–6 June. As the latter occurs, the pressure gradient increases as a katabatic surge develops over the shelf. Carrasco and Bromwich (1993a) show that the surge, which extends along the southern and western portion of the shelf from the Siple Coast to the Ross Sea, is marked by a dark (warm) signature of a few hundred kilometers in width on thermal infrared satellite imagery. As the surge develops, the average daily wind speed increases to 13.6 m s^{-1}, which is 8.2 m s^{-1} above the monthly average speed, on 5 June at AWS 8 located at 82.59°S, 174.27°W, about 200 km northeast of the Transantarctic Mountains.

Figure 9 shows the sea level pressure field produced by MM4 for 0000 UTC June 4 and 0000 UTC June 6. The MM4 simulates some of the observed features of the katabatic surge, although the intensity of the pressure gradient tends to be weaker in E1 than in the analyses shown in Fig. 8c as the simulated low remains farther to the north of the Ross Sea. Nevertheless, lowest-level wind speed approximately doubles over a period of 24 h to about 8 m s^{-1} at 0000 UTC 6 June for the eastern half of the shelf. Consequently, turbulent heat flux from the atmosphere to the surface increased, and minimum surface temperature over the center of the shelf rose from 219.9 to 224.2 K during 1200 UTC 5 June–0000 UTC 7 June.

Studies have examined regional influences on cyclones in high southern latitudes. Carrasco and Bromwich (1993b) have studied the frequent mesoscale cyclogenesis over the Ross Sea. They found that the cyclogenesis is associated with local baroclinic zones and the intensity of the katabatic wind blowing from Terra Nova Bay. Furthermore, Kottmeier et al. (1993) discuss the bounds placed on cyclone flows by the steep Antarctic topography. The development of the frontal cyclone near 150°W in E1 is influenced by topography. The simulation produces a warm front extending east from the low center at 0000 UTC 6 June (Fig. 10). Confluence is seen along the front as easterly flow along the coast is met by northeasterly flow directed from over open water. By employing a mesoscale model, we can see the detailed mesoscale structure of cyclones and confluence zones in the vicinity of Antarctica, while synoptic analyses of these events are limited by the sparsity of observations in high southern latitudes.

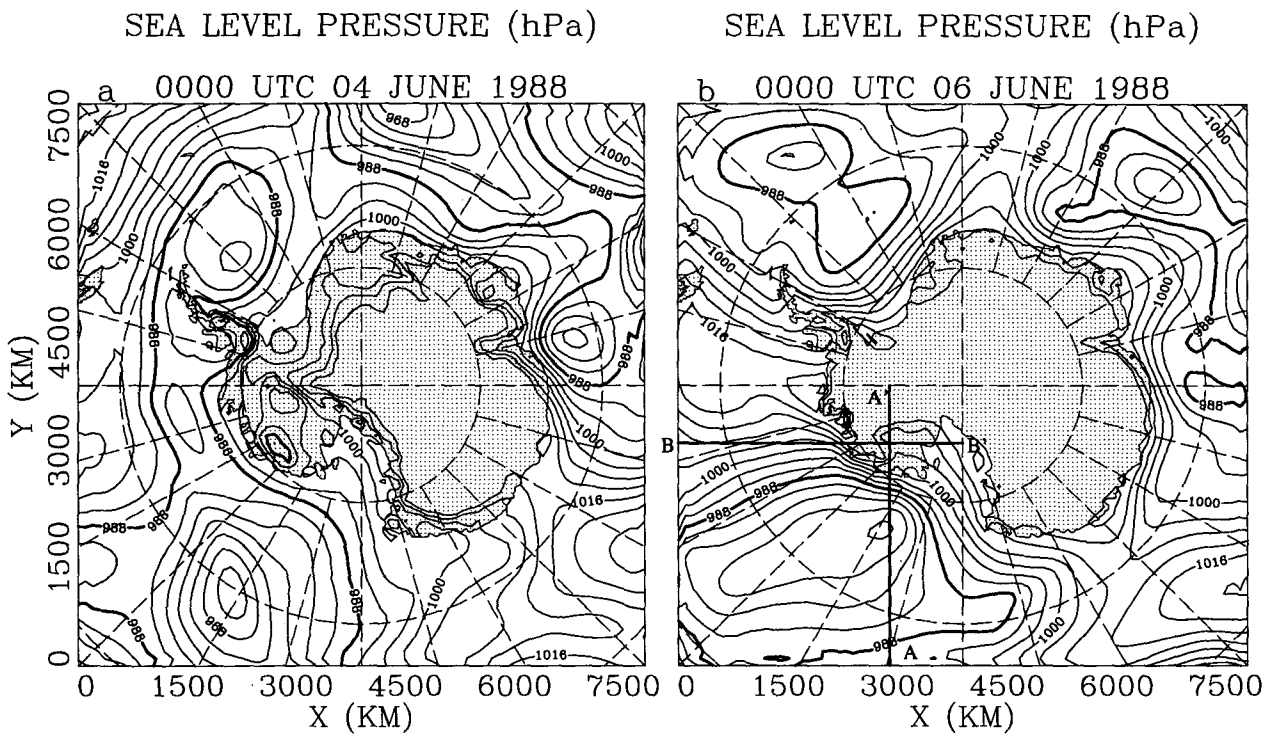

FIG. 9. As in Fig. 8 except for E1 at (a) 0000 UTC 4 June and (b) 0000 UTC 6 June 1988. Thick solid lines in (b) are the location of the cross sections in Fig. 11. Thick contour is 988 hPa.

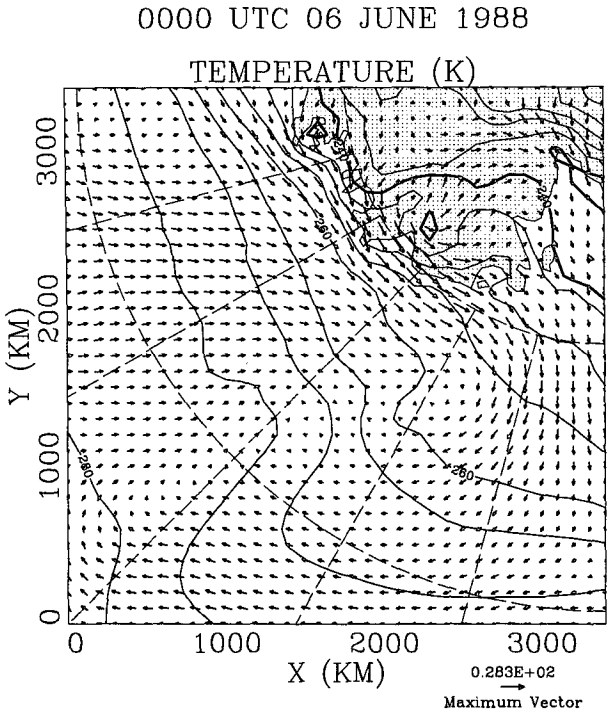

FIG. 10. Regional map of temperature (K, solid lines) and horizontal velocity (m s^{-1}, arrows) at 0000 UTC 6 June 1988 for E1. Contour interval for temperature is 5 K. Thick contour is 240 K.

As Fig. 10 shows, the low-level flow just offshore from West Antarctica is strong easterly and parallel to the coast. Yet the 500-hPa wind field at this time (not shown) has a large onshore component associated with the intense ridge to the east. The cross section in Fig. 11a shows warm lower-tropospheric air next to the coastal mountains as the flow is wrapping around the surface low. Farther to the east, cold-air damming occurs against the coastal mountains (Fig. 11b). Observations of the coastal velocity at Russkaya station (74.8°S, 136.9°W) show strong easterly flow of 30 and 60 kt, respectively, at 0000 UTC 7 June and 0000 UTC 8 June. The strong easterlies develop earlier in E1 than in the observations, as the simulation did not capture accurately enough the development of the eastward propagating low at the surface.

Although E1 captures many observed features of the period, the simulation appears to fare poorly in the vicinity of the Antarctic Peninsula. An observed low deepens from 977 hPa at 0000 UTC 4 June to 958 hPa at 1200 UTC June 5 as it propagates eastward from just west of the Antarctic Peninsula toward the Weddell Sea. Figure 8 shows the low centered to the north of the Weddell Sea at 0000 UTC 6 June, when the central pressure was 961 hPa. The eastward propagation of the simulated low lags that of the analyzed low. Furthermore, the simulation has not captured the intensification of the low as the central pressure is overestimated by 21 hPa at this time. In addition to the sensible heat flux parameterization discussed previously, inadequate representation of the narrow mountain range along the peninsula can contribute to the model's deficiency near this region. Moreover, Schwerdtfeger and Komro (1978) discuss baroclinity associated with the cold barrier winds as a key factor in the observed deepening of a southeastward propagating low to the north of the peninsula. Thus, the barrier winds may have produced or enhanced the deepening of the low seen in Fig. 8 as it moved east of the peninsula.

In summary, MM4 has demonstrated some success in capturing synoptic features during simulation E1. Mesoscale features resulting from the steep coastal mountains are represented in the simulation.

c. *June 1988 simulation*

To further evaluate the viability of MM4 for climate studies of high southern latitudes, a month-long simulation for June 1988 is performed. This simulation, hereby referred to as E2, represents the period from 0000 UTC 1 June to 0000 UTC 1 July. The specifications for this simulation are otherwise similar to that of the previous simulation E1. The average 500-hPa height fields over the month-long simulation and from the ECMWF analyses are shown in Fig. 12. Also plotted in Fig. 12a are 500-hPa heights obtained using the method of Phillpot (1991) for three AWS locations: Clean Air (South Pole), Dome C, and D-80. His method is based on the high correlation of 500-hPa height to observed surface air pressure and temperature for high elevation weather stations over Antarctica. The analyzed and simulated height fields over the high plateau of Antarctica correspond well to the 500-hPa heights estimated with Phillpot's method. Both the simulation and the analyses indicate height gradients over Antarctica are very weak. Larger gradients are concentrated in the westerlies north of 60°S, slightly more so in E2 than in the analyses. Three major lows, near 15°W, 60°E, and 160°W, are seen in the analyses. Lows of essentially the same location and central height are also seen in E2. Differences between simulated and analyzed height are largest near the analyzed ridges (Fig. 12c). Nevertheless, differences never exceed about 60 m. The simulated ridge over the high plateau of East Antarctica is better defined than that in the analyses. The estimated 5065-m height from D-80 observations does suggest that the ridge may be too weak in the analyses. The weak ridges analyzed near the Antarctic Peninsula and near 40°E, respectively, are not clearly seen in the model results. Overall, the month-average fields displayed in Figs. 12a and 12b are quite similar.

The temperature field at 500 hPa shows less similarity between the month-long averages of the simulation and analyses (see Fig. 13). Simulated and analyzed minima are 231 K over Antarctica. The area of reduced gradient near Antarctica, however, extends farther over

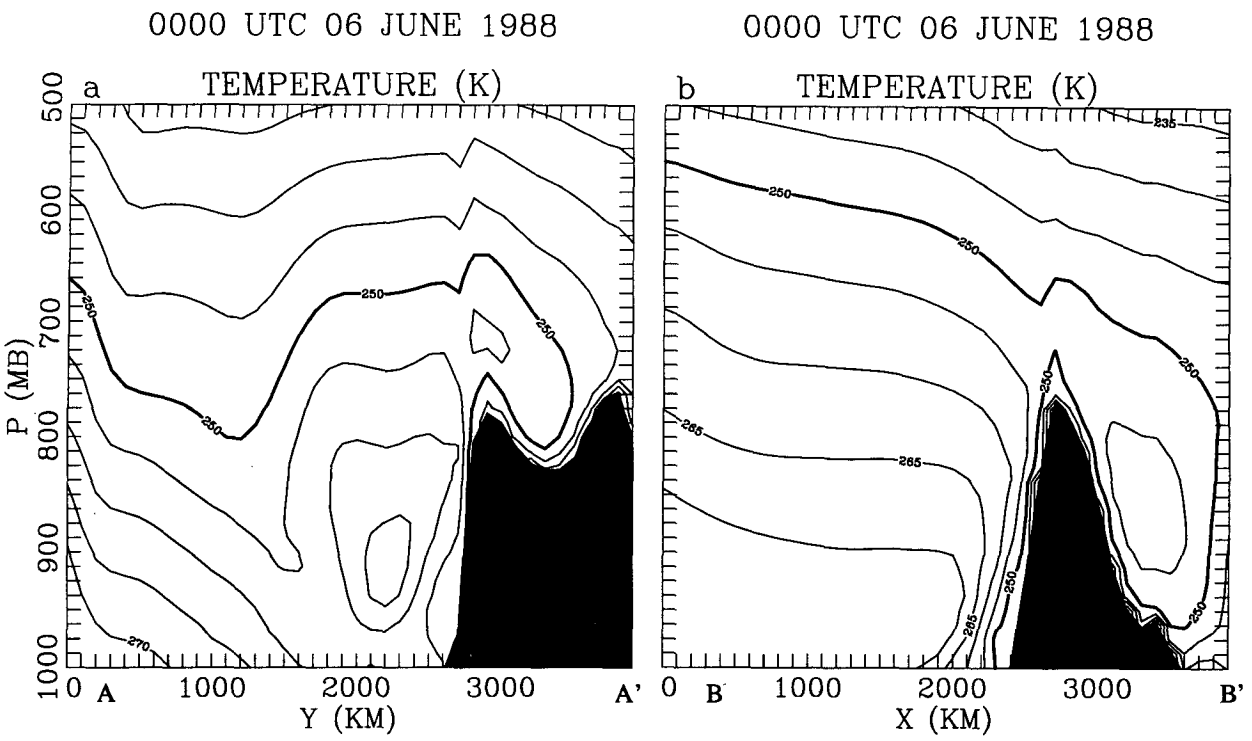

FIG. 11. Cross sections of temperature (K, solid lines) at 0000 UTC 6 June 1988 for E1 along (a) *AA'* and (b) *BB'* sketched in Fig. 9b. Contour interval is 5 K. Thick contour is 250 K.

the adjacent oceans in E2 than in the analyses. Analyzed 500-hPa temperature should be considered reliable along much of the coast of East Antarctica as data are available from several radiosonde stations. Thus, the cloud-free version of MM4 is underpredicting the middle-tropospheric temperature along the coasts and, especially, north of the Amundsen Sea. The lack of latent heating is the likely cause of the undersimulated temperatures in the middle troposphere.

The time-averaged sea level pressure fields for E2 and the analyses are shown in Fig. 14. The MM4 places the central location of the lows near 0° and 80°E within 10° longitude of their respective locations in the analyses. The broad low extending from near 180° to 75°W is split into two minima in the analyses and concentrated toward the center in E2. The oceanic lows are clearly deeper in the analyses than in E2. This is probably related to weaker cyclogenesis due to lack of latent heating in the simulation. Note that in Fig. 13c the maximum temperature difference between E2 and the analyses is located above a minimum in sea level pressure. In general, the model overpredicts the sea level pressure over the oceans. The ridge east of the peninsula, however, is more well defined in Fig. 14a for the analyses than in Fig. 14b for the simulation.

Figure 15 presents regional fields of time-averaged temperature and sea level pressure in the vicinity of the Ross Ice Shelf. Basic features of mesoscale variation in winter climate over the shelf are seen in Fig. 15a, which is derived from observations by an AWS network (Stearns et al. 1993). Model temperature in Fig. 15b is interpolated linearly in height to 3 m from values at the surface and the lowest atmospheric level. Notable observed features during June 1988 include relatively warm temperatures and multiple katabatic surges over the shelf (Stearns et al. 1993; Carrasco and Bromwich 1993a). At the warmer western edge of the shelf, in the path of the barrier flow parallel to the Transantarctic Mountains, AWS 15 reports a monthly average of −28.2°C. To the east, temperatures are colder with AWS 25 reporting −35.3°C. The simulation captures the east–west variation over the shelf, although a slight cold bias is evident. An excessive inversion strength would be expected due to the absence of downward longwave radiation from clouds. The absence of latent heating in the middle troposphere may also contribute to the model's cold bias. Above the inversion at 700-hPa, simulated temperatures (not shown) are about 2°–4°C colder than those of the ECMWF analyses (not shown) in this region.

The results of E2 appear to capture the mesoscale high on the western edge of the shelf near Mulock and Byrd Glaciers. Moreover, both panels in Fig. 15 show a southwestward sea level pressure gradient over the shelf. The analysis, based on AWS data, indicates a strong pressure gradient is toward the northern edge of

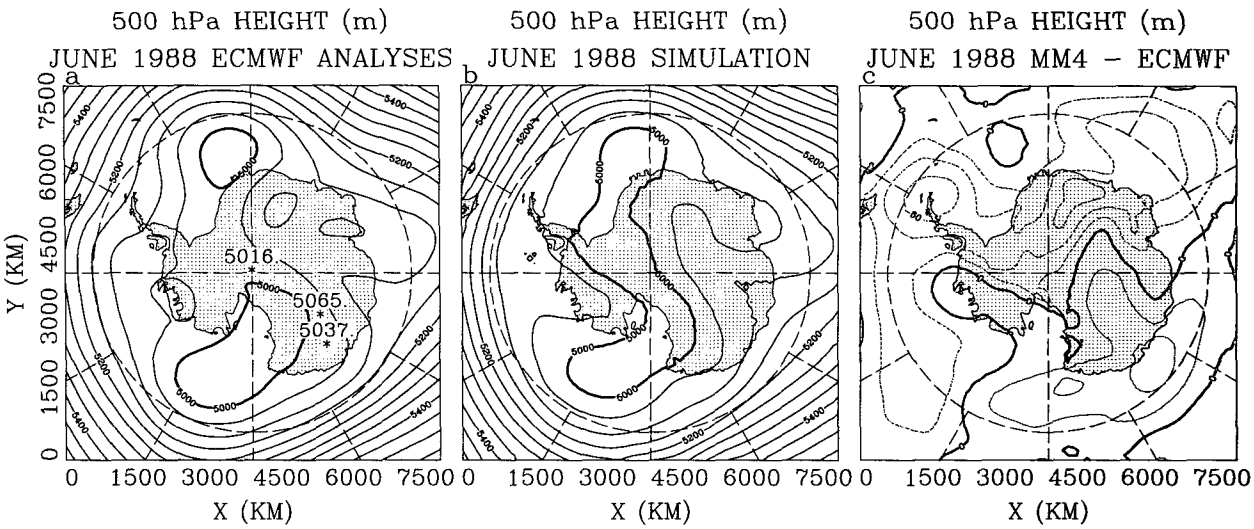

FIG. 12. Maps of 500-hPa geopotential height (m, contours) averaged over June 1988 from (a) ECMWF analyses, (b) E2, and (c) difference E2 − ECMWF analyses. Contour interval is 50 m for (a) and (b) and 20 m for (c). Thick contours are 0 m and 5000 m. Negative contours are dashed in (c). Estimated 500-hPa height following Phillpot (1991) is displayed for three AWS sites in (a).

the shelf, while the model results of MM4 produce the strongest gradient over the western part of the shelf where simulated wind speed is about 10 m s^{-1}.

Additional comparison of the time-averaged fields from the results of E2 and AWS observations is presented in Table 2. Wind direction and directional constancy of the model's lowest level, as well as the 3-m AGL values of vertically interpolated temperature and vertically extrapolated resultant wind speed, are horizontally interpolated to 10 AWS locations. These locations are selected so as to minimize the influence of finescale topography on the observations. Directional constancy is defined as the ratio of resultant wind speed to mean wind speed. The 3-m AGL speeds are extrapolated from the model's lowest level by assuming a logarithmic profile in the vertical and $z_0 = 0.0002$ m (Budd et al. 1966). Based upon a height of 22 m AGL, lowest-level winds are, thus, adjusted by a factor of 0.828.

Overall, the model results agree reasonably well with the AWS observations in Table 2. Simulated 3 m AGL temperature is within 3°C of that observed at seven stations: Clean Air (South Pole), Dome C, D-80, D-57, Lynn, Lettau, and Martha II. The simulated temperature is slightly greater than 5°C colder than the observations at stations D-10 and Elaine. Overall, the results

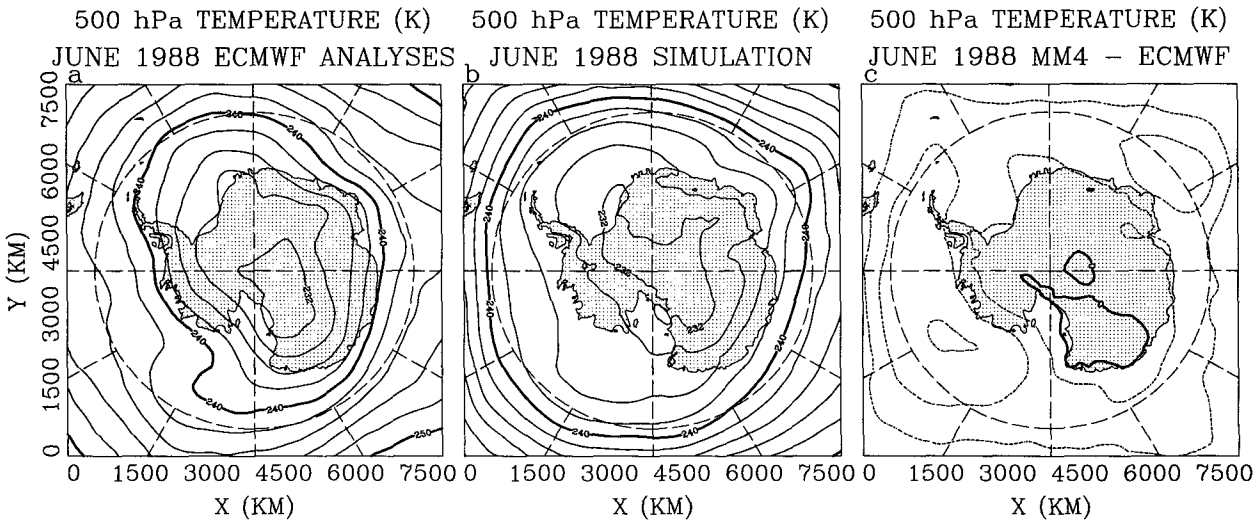

FIG. 13. As in Fig. 12 except for temperature (K). Contour interval is 2 K. Thick contours are 0 and 240 K.

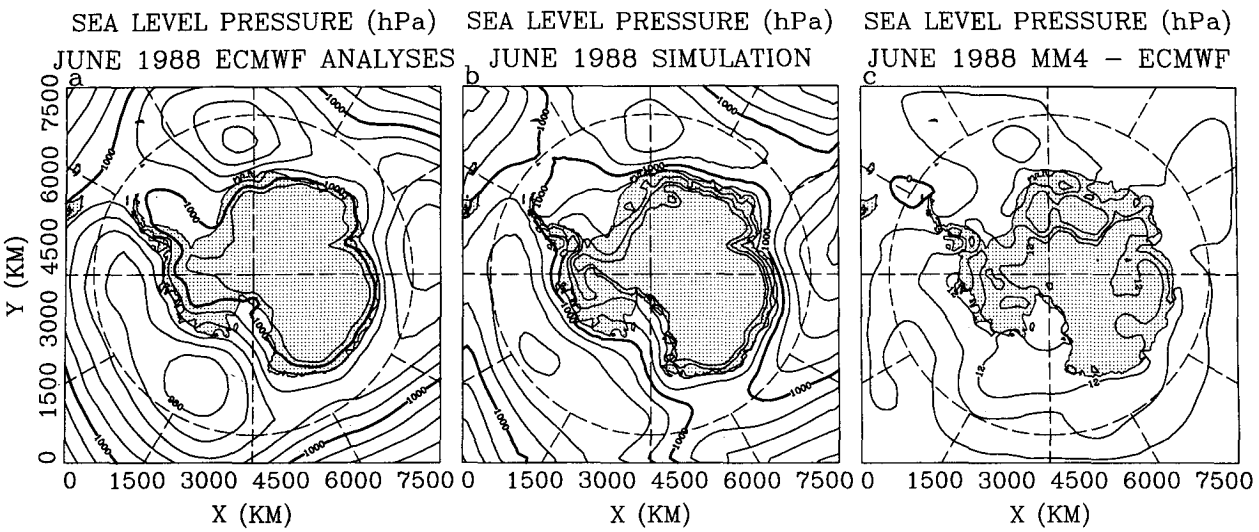

FIG. 14. As in Fig. 12 except for sea level pressure (hPa). Contour interval is 4 hPa. Thick contour is 1000 hPa. Contours are suppressed over high terrain.

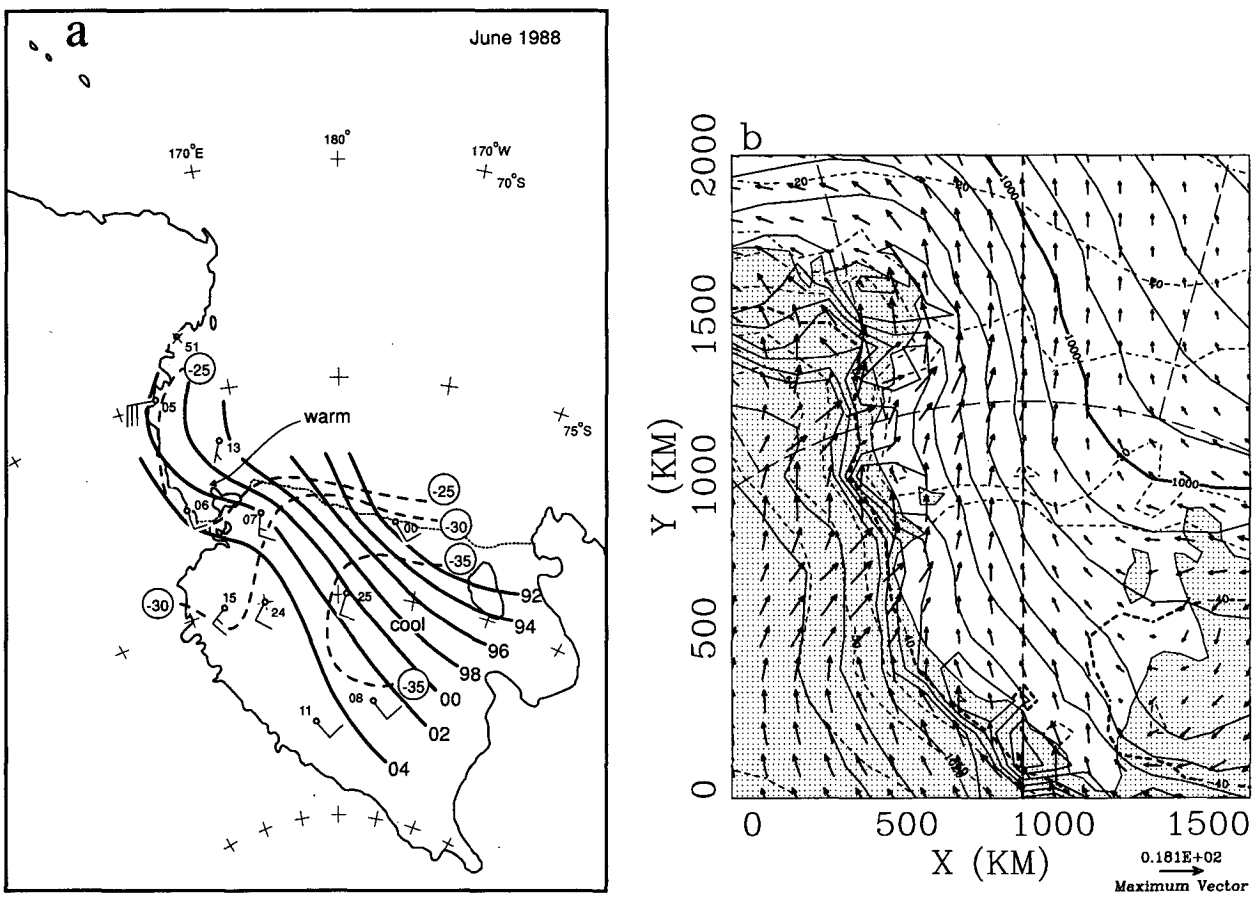

FIG. 15. Maps of sea level pressure (hPa, solid lines) and temperature at a 3-m altitude (°C, dashed lines) averaged over June 1988 for the vicinity of the Ross Ice Shelf from (a) analysis based on AWS observations and (b) results of E2 including velocity (m s^{-1}, arrows) at σ = 0.996. Contour interval for pressure is 2 and 10 hPa below and above 1020 hPa, respectively. Thick solid contour in (b) is 1000 hPa. Contour interval for temperature is 5°C. Thick dashed contour in (b) is −40°C. Wind barbs in (a) show AWS (numbered circles) resultant winds.

TABLE 2. Comparison of model results with selected AWS observations averaged for June 1988.

Station	Latitude, longitude	Elevation (m)	Observed temperature (°C)	Model temperature* (°C)	Observed resultant wind speed (m s^{-1})	Model resultant wind speed** (m s^{-1})	Observed resultant wind direction (deg)	Model lowest-level resultant wind direction (deg)	Observed directional constancy	Lowest-model-level directional constancy
Clean Air	90.00°S	2835	−58.8	−61.3	3.5	6.1	62	54	0.78	0.98
Dome C (AWS-04)	74.50°S, 123.00°E	3280	−63.1	−64.5	1.9	3.9	197	198	0.76	0.80
D-80 (AWS-19)	70.02°S, 134.72°E	2500	−48.7	−49.5	7.7	7.6	164	161	0.96	0.94
D-57 (AWS-16)	68.18°S, 137.52°E	2105	−37.4	−39.2	8.9	10.2	144	162	0.85	0.96
D-10 (AWS-12)	66.70°S, 139.80°E	240	−19.5	−24.8	9.2	11.5	149	138	0.97	0.98
Lynn (AWS-27)	74.23°S, 160.37°E	1772	−42.6	−43.5	10.0	10.4	280	252	0.96	0.97
Elaine (AWS-11)	83.15°S, 174.46°E	60	−32.5	−37.8	4.0	5.5	167	171	0.78	0.96
Lettau (AWS-08)	82.59°S, 174.27°W	55	−34.5	−37.3	4.4	6.0	157	158	0.81	0.98
Gill (AWS-25)	80.00°S, 179.00°W	55	−35.3	−39.5	4.3	5.1	214	164	0.85	0.95
Martha II (AWS-00)	78.38°S, 173.42°W	18	−32.2	−34.3	4.6	3.7	152	150	0.79	0.81

* Model temperature at the surface and lowest atmospheric level is interpolated linearly in height to 3 m AGL.
** Model resultant wind speed at the lowest atmospheric level is extrapolated in height to 3 m AGL by assuming a logarithmic profile and $z_0 = 0.0002$ m.

suggest that E2 has a typical cold bias of about 2°C. The simulated resultant wind speeds are within 1 m s^{-1} of that observed at 4 of the 10 AWS stations. Apparently, there is a systematic difference in resultant speed over the Ross Ice Shelf, where the simulated winds of 3.7–6.0 m s^{-1} are mostly faster than the 4.0-4.6 m s^{-1} speeds observed. At other locations, simulated resultant speed also tends to exceed that observed. Simulated directional constancy tends to be larger than that observed, except at D-80, where the observed value is larger. Simulated and observed directional constancies are in very good agreement at stations Dome C, D-10, Lynn, and Martha II. Table 2 also shows that PBL wind direction is well simulated by the model. Difference in direction between AWS observations and model results are less than 10° at six stations. Reeves Glacier influences the flow at Lynn, where the simulated and observed direction differ by 28°. The large westerly component observed at Gill is anomalous.

Now, we further examine the simulated PBL in E2. Figure 16 shows the month-long average of surface and lowest-level temperature. As expected, the minimum surface temperature is located near the top of the East Antarctic plateau. The minimum, 198 K near the 4000-m elevation, appears realistic since observed multiyear average temperatures for June are 204 K at 3625 m and 208 K at 3488 m, respectively, for Plateau station and Vostok (Schwerdtfeger 1984). Interestingly, the minimum for the model's lowest atmospheric level, at about 20 m AGL, is not over the top of the plateau but is near the South Pole. This is related to the horizontally varying intensity of the radiation inversion displayed in Fig. 17. The intensity of the inversion is measured here by the excess over the surface temperature of the atmospheric temperature maximum nearest to the surface. Near the top of the plateau, the surface is more than 35 K cooler than air above the inversion. Based upon available observations of atmospheric temperature, winter inversion strength over Antarctica has been analyzed by Phillpot and Zillman (1970) and updated by Schwerdtfeger (1984, see his Fig. 2.5). They found that the maximum intensity, about 25 K, is located over the East Antarctic plateau. Analyzed intensity decreases toward the coast. The maximum inversion strength in E2 is considerably larger than that in their analyses. A somewhat stronger inversion is expected in the simulation due to the lack of radiative effects from clouds. Furthermore, measured near-surface air temperature is likely to be warmer than surface temperature during winter. Significantly increased detail is displayed for the inversion intensity in Fig. 17. The simulated and analyzed inversions are relatively weak in the southeasterly flow at the southern and western edges of the Ross Ice Shelf. Inversion intensity in E2, however, exceeds 20 K in the eastern portion of the shelf. An inversion of modest intensity, usually less than 10 K, is also simulated over the flat Filchner/Ronne Ice Shelf. Radiation inversions are largely non-

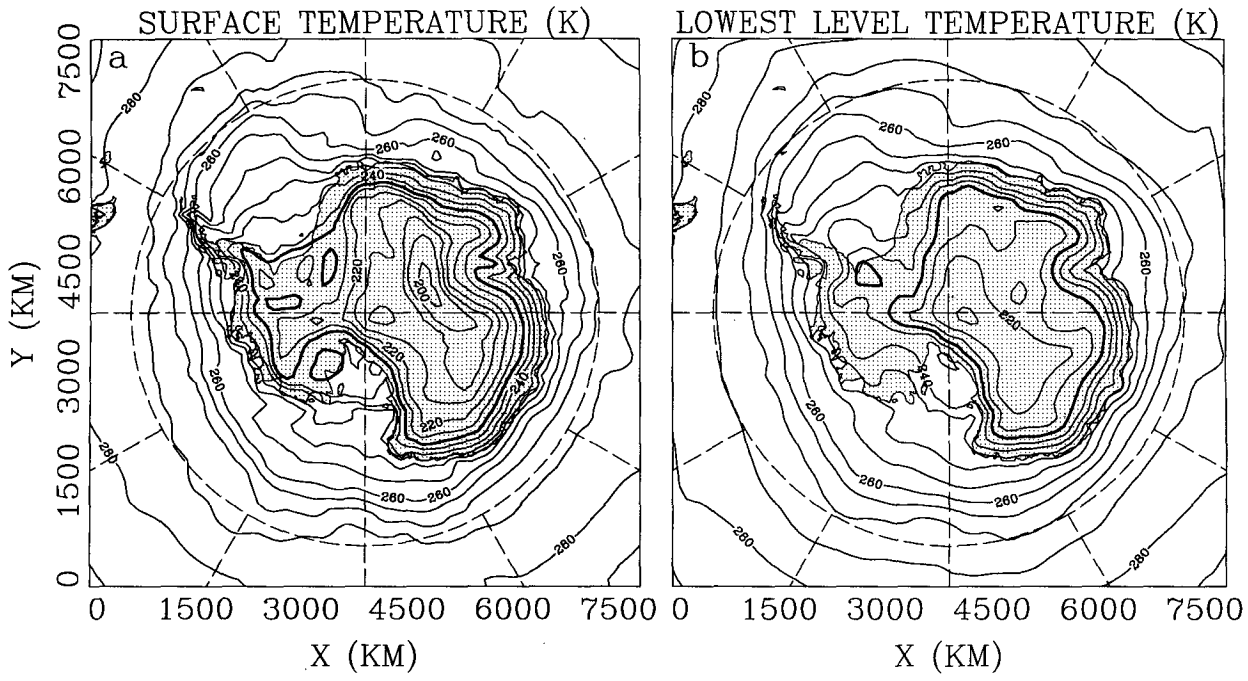

FIG. 16. Temperature (K, solid line) from E2 averaged over June 1988 at (a) the surface and (b) $\sigma = 0.996$. Contour interval is 5 K. Thick contour is 230 K.

existent over the open oceans as the water is a source of heat to the atmosphere in the austral winter for high southern latitudes.

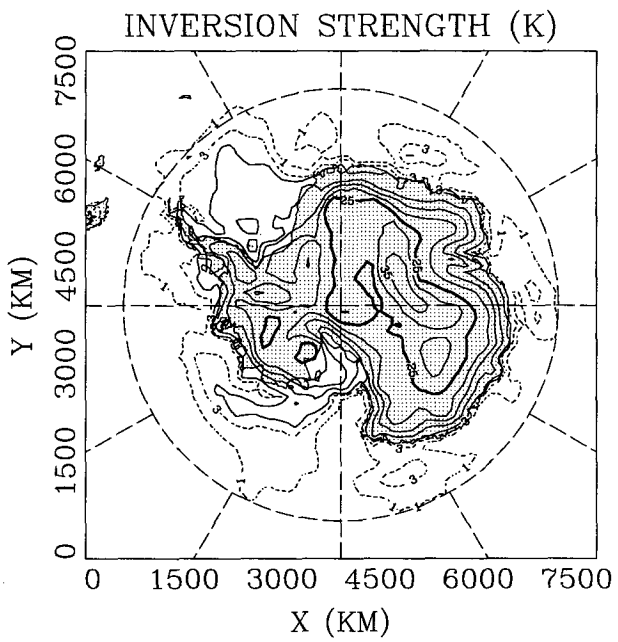

FIG. 17. Surface inversion strength (K, contours) from E2 averaged over June 1988. Solid contour interval is 5 K. Thick solid contour is 25 K. Dashed contours are 1 and 3 K.

Lowest-model-level wind velocity for June 1988 is displayed in Fig. 18a. The wind direction pattern for E2 over Antarctica is essentially identical to that for idealized simulations PW1 and PB1 (Fig. 4). Parish and Bromwich (1987, 1991) provided representations of the streamlines over the Antarctic ice surfaces. Figure 18a has added a representation of the velocity field over the nearby oceans extending out to the band of westerlies north of 60°S. Over the oceans, PBL flow converges into centers of low pressure. Note from Fig. 16a that the minimum surface temperature over the plateau is very near the center of the continent-wide difluence pattern. A distinct feature of the velocity pattern is the strong southerly winds that extend downstream off the Ross Ice Shelf for about 1000 km over and beyond the Ross Sea. On the other hand, the barrier wind pattern often observed near the western edge of the Weddell Sea is again quite weak in the simulation.

Simulated low-level wind speeds in E2 are stronger than those seen in the results of idealized simulation PB1. This emphasizes the significance of mechanical forcing of boundary layer turbulence by the synoptic-scale wind. The Adélie Coast near 140°E is noted for the intensity of its katabatic winds. Simulated monthly average wind speeds along the coast of East Antarctica from 110° to 145°E are typically greater than 10 m s^{-1}, with a maximum of 14.4 m s^{-1} near 135°E. Faster simulated winds occur along the Princess Ragnhild Coast near 30°E. Maximum lowest-level speed is 19.4 m s^{-1} there. Maxima of the coastal winds are typically 2–3

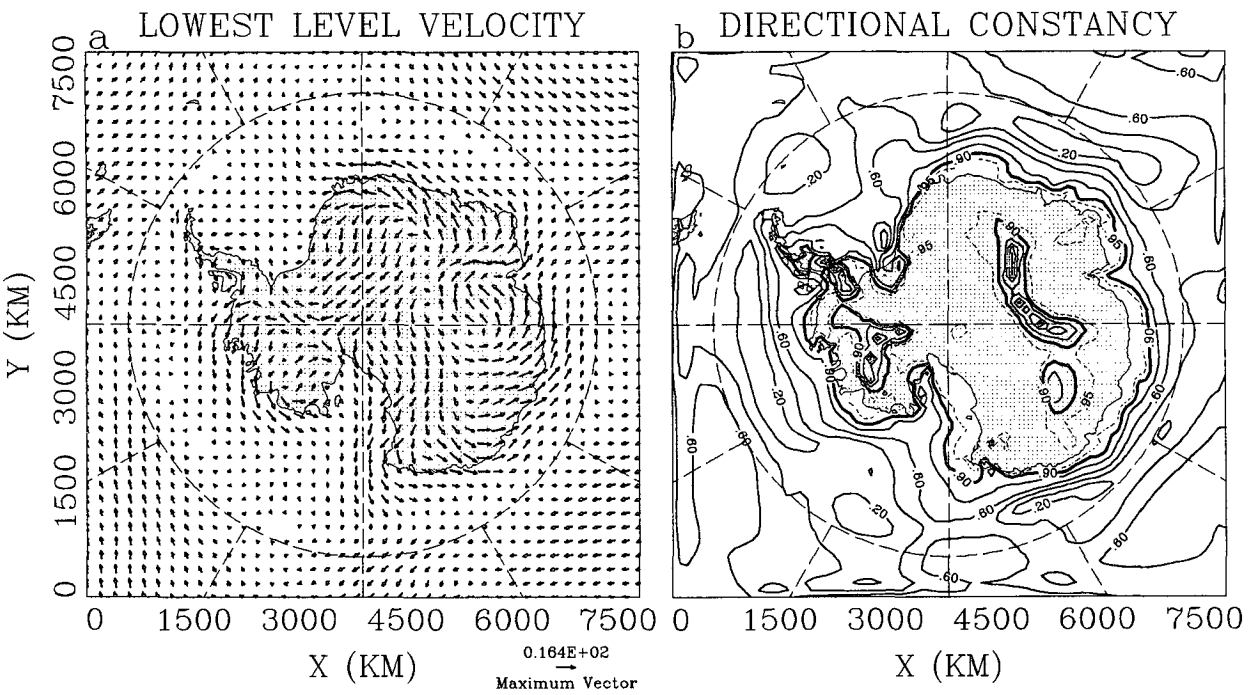

FIG. 18. Maps of (a) resultant wind vectors (m s^{-1}, arrows) and (b) directional constancy (contours) for σ = 0.996 from E2. Solid contour interval is 0.2 up to 0.8. Thick solid contour is 0.9. Dashed contour is 0.95.

m s^{-1} larger for the model's next highest level at about 85 m AGL. Figure 18a also shows that near the center of the trough surrounding Antarctica monthly average velocities are quite small. Monthly average wind speeds, however, exceed 10 m s^{-1} over most of the ocean surface north of 55°S.

The steadiness of the drainage pattern over Antarctica is demonstrated by the very high directional constancy of the boundary layer flow over much of the continent. At Antarctic stations, where the mean speed is large, directional constancy over a year normally exceeds 0.8 (Schwerdtfeger 1984). Directional constancy exceeded 0.95 at several AWS sites during June 1988 (Stearns et al. 1993). Figure 18b displays the directional constancy of the lowest-level winds taken at 12-h intervals. Over most of Antarctica, values are quite large, exceeding 0.95. Over the oceans, directional constancy is considerably smaller, largely due to the influence of migrating cyclones. Nevertheless, the simulated directional constancy does exceed 0.75 in localized regions within the band of westerlies.

4. Conclusions and future work

A mesoscale atmospheric model, a modified form of The Pennsylvania State University–NCAR MM4 is used to simulate the winter climate of high southern latitudes. The simulations test the viability of the mesoscale model for regional and GCM coupled climate studies. The model has the capability to capture mesoscale features of the frequent cyclones over the oceans near Antarctica, as well as 3D features of the winter Antarctic boundary layer, which are very poorly resolved in observations and often inadequately resolved by GCMs.

Results of MM4 are compared with those of a modified version of the mesoscale model of Parish and Waight (1987), which has been shown to simulate the katabatic winds of Antarctica quite well. The longwave radiation scheme and components of the PBL parameterization used by PW are incorporated into the version of MM4 used here. Simulations with the two models demonstrate the sensitivity of the katabatic layer to parameterization of the turbulent fluxes. These results indicate that MM4 produces similar katabatic wind patterns, albeit with speeds tending to be somewhat weaker, compared to those simulated by PW under simple, idealized conditions. Some forcing of turbulence was required in the idealized run PB1 to adequately simulate the katabatic wind pattern. In more realistic simulations, using ECMWF analyses for initial and boundary conditions, the synoptic flow generates turbulence and, thus, katabatic winds are adequately simulated.

Simulations of Antarctic winter conditions based upon ECMWF analyses for June 1988 and climatological sea-ice distributions demonstrate that MM4 well simulates many synoptic and climatological features for the vicinity of Antarctica. Although the focus of this study is primarily on the climatological aspects of

the simulations, nevertheless, MM4 has performed well over a 6-day simulation. The mesoscale model successfully predicts the development of a ridge over East Antarctica and features of a katabatic surge over the Ross Ice Shelf. Model results are poor, however, in the vicinity of the Antarctic Peninsula. Simulated winter climatology is evaluated by comparing the results of a month-long simulation for June 1988 with time-averaged ECMWF analyses. The climatological 500-hPa height field is well produced in the simulation. The location, but not the intensity, of the climatological oceanic lows are also well produced by MM4. Furthermore, the month-averaged temperature and velocity agree reasonably well with AWS observations.

The success of the completely cloud-free simulations indicate that the winter Antarctic climate is largely controlled by dry dynamics. However, the lack of latent heating and longwave radiation from clouds may result in weaker cyclones over the oceans and excessively cold temperatures and excessive inversion strength in some locations over Antarctica. The natural extension of this work involves examining the influence of moist processes in Antarctic climatology. It is expected that the inclusion of latent heating in the simulations will improve the forecast of the intensity of oceanic cyclones and, thereby, produce a more intense circumpolar trough surrounding Antarctica. Another improvement in the simulations, particularly near the Antarctic Peninsula, should be achievable with a better parameterization of the sensible heat flux. Furthermore, the accumulation of ice over Antarctica is a critical component in the global climate and water balance. Future simulations should, therefore, evaluate the forecast of precipitation over the Antarctic ice sheets with a model adequately resolving the key topographic forcing. Finally, as variability of sea ice is considered an important component of climate variability in high latitudes, simulations should be performed with observed sea-ice concentrations from Special Sensor Microwave/Imager (SSM/I) data.

Acknowledgments. We greatly appreciate the programming assistance of Larry Oolman and Ren-Yow Tzeng, as well as the assistance of Jorge Carrasco, Beth Daye, and John Nagy in the preparation of the figures. This research is supported by a fellowship of the University Corporation for Atmospheric Research's Climate System Modeling Program, by NASA via grant NAGW-2718 to DHB, and by the National Science Foundation (NSF) via grant DPP-9117202 to TRP. The numerical simulations were performed on the CRAY-YMP of the Ohio Supercomputer Center, which is supported by the state of Ohio, and on the CRAY-YMP of NCAR, which is supported by NSF.

REFERENCES

Anthes, R. A., E.-Y. Hsie, and Y.-H. Kuo, 1987: Description of The Pennsylvania State/NCAR mesoscale model version 4 (MM4). NCAR Technical Note, NCAR/TN-282 + STR, 66 pp.

Arakawa, A., and V. R. Lamb, 1977: Computational design of the basic dynamical processes of the UCLA general circulation model. *Methods in Computational Physics,* Academic Press, 173–275.

Ball, F. K., 1960: Winds on the ice slopes of Antarctica. *Antarctic Meteorology, Proceedings of the Symposium in Melbourne, 1959,* Pergamon Press, 9–16.

Blackadar, A. K., 1979: High resolution models of the planetary boundary layer. *Advances in Environmental Science and Engineering.* Vol. 1, No. 1, J. Pfafflin and E. Ziegler, Eds., Gordon and Breach, 50–85.

Bromwich, D. H., 1991: Mesoscale cyclogenesis over the southwestern Ross Sea linked to strong katabatic winds. *Mon. Wea. Rev.,* **119,** 1736–1752.

——, Y. Du, and T. R. Parish, 1994: Numerical simulation of winter katabatic winds from West Antarctica crossing Siple Coast and the Ross Ice Shelf. *Mon. Wea. Rev.,* **122,** 1417–1435.

Brost, R. A., and J. C. Wyngaard, 1978: A model study of the stably-stratified planetary boundary layer. *J. Atmos. Sci.,* **35,** 1427–1440.

Budd, W. F., W. Dingle, and U. Radok, 1966: The Byrd snowdrift project: Outline and basic results. *Studies in Antarctic Meteorology, Antarctic Research Series.* Vol. 9, M. Rubin, Ed., American Geophysical Union, 71–134.

Businger, J. A., J. C. Wyngaard, Y. Izumi, and E. F. Bradley, 1971: Flux-profile relationships in the atmospheric surface layer. *J. Atmos. Sci.,* **28,** 181–189.

Carrasco, J., and D. H. Bromwich, 1993a: Satellite and automatic weather station analyses of katabatic surges across the Ross Ice Shelf. *Antarctic Meteorology and Climatology: Studies Based on Automatic Weather Stations, Antarctic Research Series.* Vol. 61, D. H. Bromwich and C. R. Stearns, Eds., American Geophysical Union, 93–108.

——, and ——, 1993b: Mesoscale cyclogenesis dynamics over southwestern Ross Sea. *J. Geophys. Res.,* **98,** 12 973–12 995.

Cerni, T. A., and T. R. Parish, 1984: A radiative model of the stable nocturnal boundary layer with application to the polar night. *J. Climate Appl. Meteor.,* **23,** 1563–1572.

Drewry, D. J., 1983: The surface of the Antarctic ice sheet. *Antarctica: Glaciological and Geophysical Folio,* sheet 2, D. J. Drewry, Ed., Scott Polar Research Institute, Cambridge.

Giorgi, F., and G. T. Bates, 1989: The climatological skill of a regional model over complex terrain. *Mon. Wea. Rev.,* **117,** 2325–2347.

——, C. S. Brodeur, and G. T. Bates, 1994: Regional climate change scenarios over the United States produced with a nested regional climate model. *J. Climate,* **7,** 375–399.

James, I. N., 1988: On the forcing of planetary-scale Rossby waves by Antarctica. *Q. J. Roy. Met. Soc.,* **114,** 619–637.

Kottmeier, C., P. Wachs, and K. Sannemann, 1993: Coastal Antarctic PBL flows under varying external influences. *Waves and Turbulence in Stably Stratified Flows,* Clarendon Press, Oxford, 61–89.

Mather, K. B., and G. S. Miller, 1967: Notes on the topographic factors affecting the surface wind in Antarctica, with special reference to katabatic winds, and bibliography. Rep. UAG-189, Geophysical Institute, University of Alaska, Fairbanks, 25 pp.

Parish, T. R., 1992: On the interaction between Antarctic katabatic winds and tropospheric motions in the high southern latitudes. *Aust. Met. Mag.,* **40,** 149–167.

——, and D. H. Bromwich, 1987: The surface wind field over the Antarctic ice sheets. *Nature,* **328,** 51–54.

——, and K. T. Waight, 1987: The forcing of Antarctic katabatic winds. *Mon. Wea. Rev.,* **115,** 2214–2216.

——, and D. H. Bromwich, 1991: Continental-scale simulation of the Antarctic katabatic wind regime. *J. Climate,* **4,** 135–146.

Phillpot, H. R., 1991: The derivation of 500 hPa height from automatic weather station surface observations in the Antarctic continental interior. *Aust. Met. Mag.,* **39,** 79–86.

——, and J. W. Zillman, 1970: The surface temperature inversion over the Antarctic continent. *J. Geophys. Res.*, **75,** 4161–4169.

Pitman, A. J., F. Giorgi, and A. Henderson-Sellers, 1991: Southeast Australia's wintertime precipitation: Sensitivity of climate predictions to model resolution. *Aust. Met. Mag.*, **39,** 21–35.

Schwerdtfeger, W., 1979: Meteorological aspects of the drift of ice from the Weddell Sea toward the mid-latitude westerlies. *J. Geophys. Res.*, **84,** 6321–6328.

——, 1984: *Weather and Climate of the Antarctic.* Elsevier Science, 261 pp.

——, and F. Komro, 1978: Early winter storms in the northwestern Weddell Sea. *Antarct. J. U.S.*, **13,** 175–177.

Stearns, C. R., and G. A. Weidner, 1993: Sensible and latent heat flux estimates in Antarctica. *Antarctic Meteorology and Climatology: Studies Based on Automatic Weather Stations, Antarctic Research Series.* Vol. 61, D. H. Bromwich and C. R. Stearns, Eds., American Geophysical Union, 109–138.

——, L. M. Keller, G. A. Weidner, and M. Sievers, 1993: Monthly mean climatic data for Antarctic automatic weather stations. *Antarctic Meteorology and Climatology: Studies Based on Automatic Weather Stations, Antarctic Research Series.* Vol. 61, D. H. Bromwich and C. R. Stearns, Eds., American Geophysical Union, 1–21.

Tzeng, R.-Y., D. H. Bromwich, and T. R. Parish, 1993: Present-day Antarctic climatology of the NCAR Community Climate Model Version 1. *J. Climate,* **6,** 205–226.

Xu, J.-S., H. von Storch, and H. van Loon, 1990: The performance of four spectral GCMs in the Southern Hemisphere: The January and July climatology and the semiannual wave. *J. Climate,* **3,** 53–70.

Yasunari, T., and S. Kodama, 1993: Intraseasonal variability of katabatic wind over East Antarctica and planetary flow regime in the Southern Hemisphere. *J. Geophys. Res.*, **98,** 13 063–13 070.

Yimin, M., 1992: Simulation of katabatic winds at Mizuho station, Antarctica. *Antarctic Research,* **3,** 25–30.

Zhang, D.-L., and R. A. Anthes, 1982: A high-resolution model of the planetary boundary layer-sensitivity tests and comparisons with SESAME-79 data. *J. Appl. Meteor.*, **21,** 1594–1609.